Supporting Information

Wang et al. 10.1073/pnas.1320235110

SI Text

Estimation of Crack Length

We extract frames from our experimental movies and then use following image-processing method to characterize the crack length:

i) We decrease the bit depth of the original jpeg picture (e.g., Fig. S4*A*) to 8-bit (Fig. S4*B*) for further image processing.
ii) We use the Sobel method (the Sobel method is usually used on edge detection in image processing by computing an approximate gradient of the image intensity function) (1) to detect the boundary of the crack. Fig. S5 shows the resulting traced notch/crack boundary.
iii) Finding the apex of the crack (point A in Fig. S6) and the bottom of the notch profile (point B in Fig. S6), we draw a line between these two points.
iv) Detecting the reference point C in the notch/crack boundary and measuring the crack length. First, the vertical distance between the point on the curved edge line and the straight line AB is automatically measured, where the peak distance corresponds to the reference point C; second, the crack length of the fatigue crack was determined as the line distance AC as seen in Fig. S7; third, after rescaling the length AC to the scale bar, we get the real length of the crack.

Molecular Dynamics Simulation

To understand the structure evolution due to the cyclic straining, molecular dynamics (MD) simulation is used to reveal atomic rearrangement processes. Simulations on a binary bulk metallic glass (BMG) system ($Al_{50}Fe_{50}$) are performed in this study.

We adopt the Al-Fe interatomic potential of Mendelev et al. (2). The configuration is produced by adopting a similar procedure: (*i*) Glass samples consisting of 2,000 atoms are prepared from a melting-and-quenching simulation of a randomly substituted solid solution in a face centered cubic (fcc) lattice, whose temperature is raised gradually from 300 K to 3,000 K, equilibrated for 1,000 ps, and cooled down to 50 K, with the effective heating and cooling rates of 0.425 K/ps. The time step for integration is chosen to be 0.002 ps. Pressure is maintained at zero during both the heating and the cooling processes. The dimensions of as-prepared glass samples are $\sim 4 \times 4 \times 2$ nm. (*ii*) The final sample with dimension of $\sim 59 \times 74 \times 2$ nm is produced by multiplying the amorphous sample produced by step *i* along the *x* and *y* axes. (*iii*) A crack with a dimension of $\sim 22 \times 2 \times 2$ nm is created in the middle of the final sample. The ensemble used in the simulation is the isothermal–isobaric ensemble with conserved moles, pressure, and temperature (NPT). During simulations, cyclic loading is applied in the *y* direction with a strain rate of $\sim 10^9$/s whereas the strain rate in the *z* axis remains zero. The deformation is carried out under displacement-controlled mode and the strain range is set to be $3 \pm 1.8\%$ for cyclic testing. The set peak strain is close to the yield point from monotonic testing ($\sim 5.8\%$) such that we could monitor the structure changes and crack evolution within a reasonable time. In our adopted NPT ensemble, the temperature is strictly controlled around 50 K (only 0.1 K fluctuation is allowed). Thus, there is no temperature effect or any significant temperature rise in our simulations. On the other hand, the external stress would enhance the translational displacement of atoms in our simulated system, although it does not have a significant contribution to atoms' random vibration. Thus, the MD simulations suggest that the nanocrystallization can be induced by externally applied cyclic stress without temperature rise.

For comparison, we also performed a monotonic loading of the model with maximum strain up to 8%. The main results are shown in Fig. S8, using Falk and Langer's method (3). We also adopt the Honey–Anderson method to characterize the crystal (4, 5).

1. Heath M, Sarkar S, Sanocki T, Bowyer K (1998) Comparison of edge detectors. *Comput Vis Image Underst* 69(1):17–22.
2. Mendelev MI, Srolovitz DJ, Ackland GJ, Han S (2005) Effect of Fe segregation on the migration of a non-symmetric Sigma 5 tilt grain boundary in Al. *J Mater Res* 20(1): 208–218.
3. Falk ML, Langer JS (1998) Dynamics of viscoplastic deformation in amorphous solids. *Phys Rev E Stat Phys Plasmas Fluids Relat Interdiscip Topics* 57(6):7192–7205.
4. Honeycutt JD, Andersen HC (1987) Molecular dynamics study of melting and freezing of small Lennard-Jones clusters. *J Phys Chem* 91(19):4950–4963.
5. Tsuzuki H, Branicio PS, Rino JP (2007) Structural characterization of deformed crystals by analysis of common atomic neighborhood. *Comput Phys Commun* 177(6):518–523.

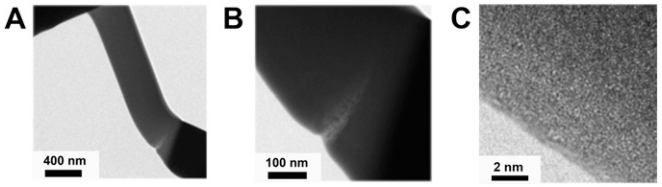

Fig. S1. The morphology of an Al-Fe metallic glass cantilever (with a total microbeam length of 2,700 nm, a middle section width of 420 nm, and a middle section thickness ~100 nm) after a monotonic bending with a displacement more than 2 μm (4.8 times the middle section width). (*A*) Extensive plastic deformation is seen in the bent specimen. (*B*) A magnified view of the highly deformed zone of the specimen where a shear band containing many nanocrystals can be seen. (*C*) High-resolution transmission electron microscope (TEM) image of the edge around the shear band after severe monotonic plastic deformation, indicating a smooth surface at the nanometer scale.

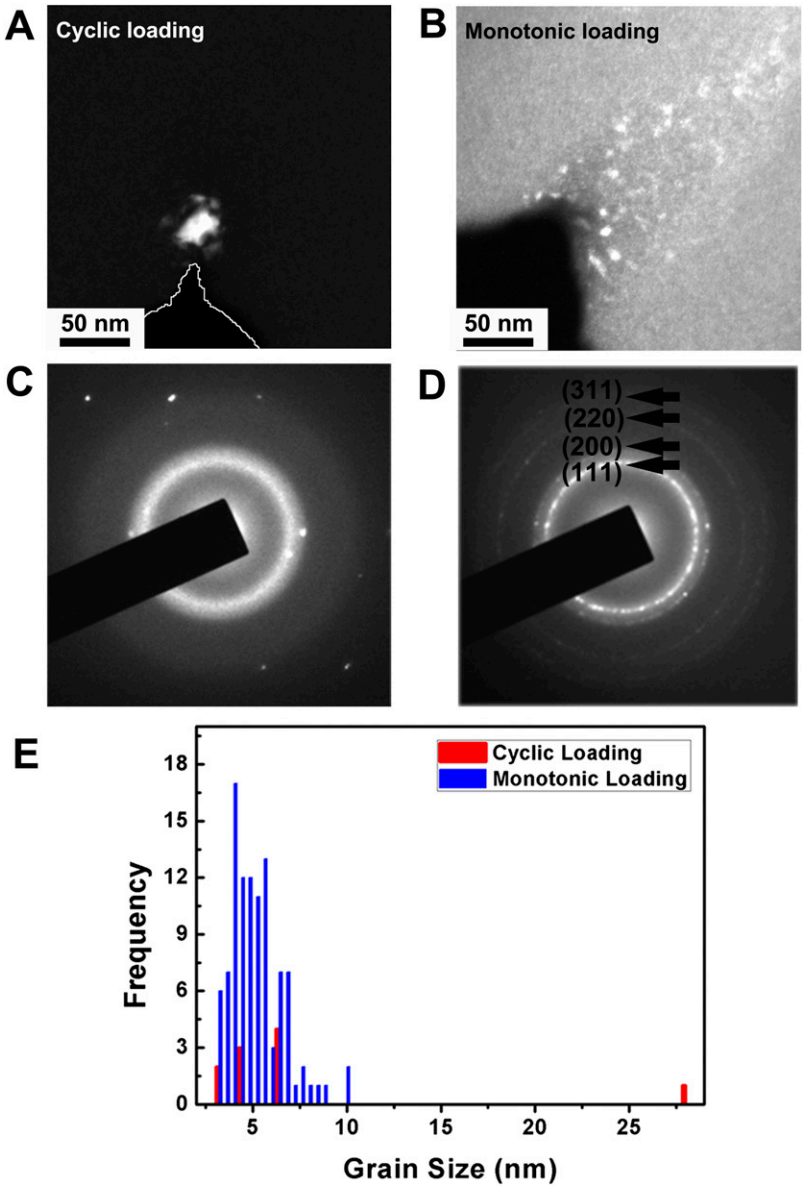

Fig. S2. Glass-to-crystal transition during cyclic and monotonic loading of metallic glass. (*A*) A large grain (~27 nm in size) with several tiny satellite grains found ahead of the fatigue crack tip after 1,500 cycles. In contrast, numerous grains smaller than 10 nm in size appeared following monotonic loading of a sample (with roughly the same initial dimensions as in Fig. S1) bent with a displacement of ~1.5 μm (about 3.6 times the middle section width). (*B*–*D*) Analyses (*B*) of the diffraction patterns (*C* and *D*) suggest that deformation-introduced crystals have a face-centered cubic structure. (*E*) The histogram of grain size vs. frequency measured in *A* and *B*.

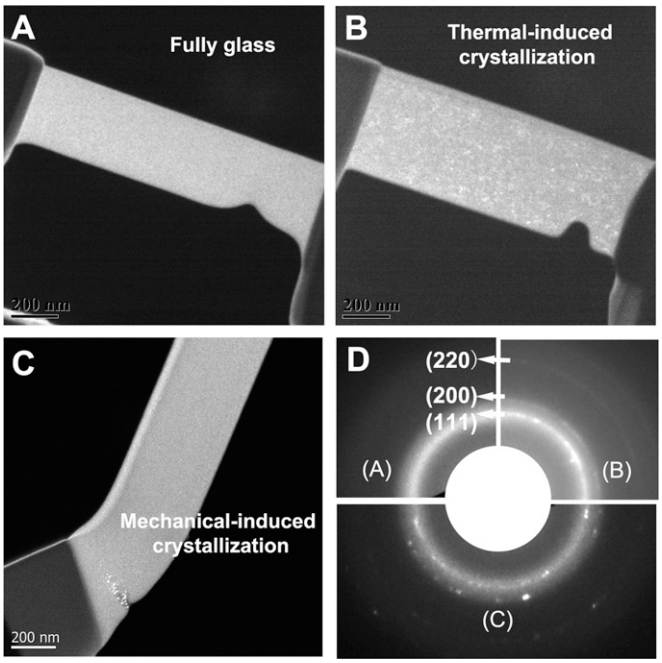

Fig. S3. Structure of mechanically induced vs. thermally induced crystal phases in Al-based metallic glass (MG) cantilevers. (*A*–*C*) Dark-field TEM images of untested, thermally treated (heated up to 150 °C for about 20 min in the air), and mechanically deformed specimens. The nanocrystals are distributed homogeneously in the specimen after thermal treatment (*B*). In contrast, crystalline phases appeared only in the plastically deformed region of the deformed specimens. (*D*) The nanocrystals, whether thermally induced or mechanically induced, all have a FCC crystal structure.

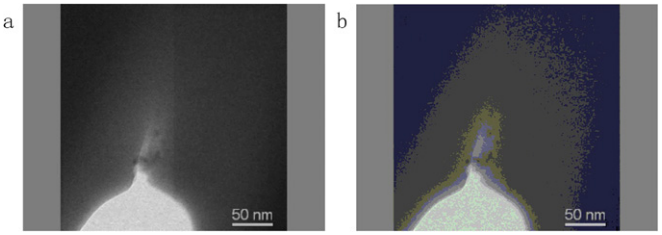

Fig. S4. (*A*) A typical original movie frame showing the notch and the crack tip. (*B*) After being converted to 8-bit from *A*.

Fig. S5. Traced notch/crack profile by applying the Sobel method.

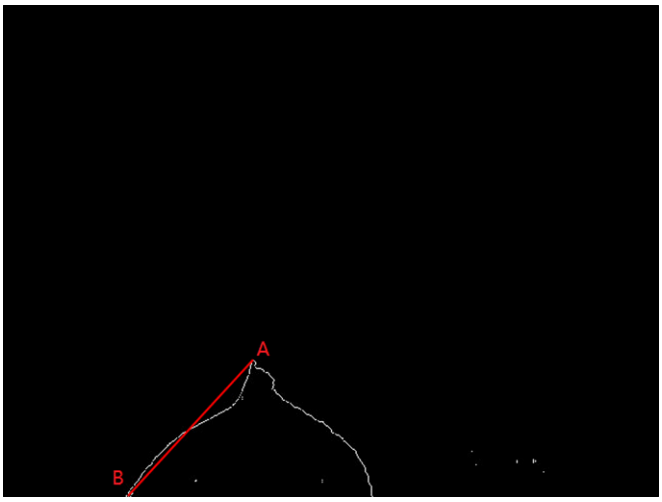

Fig. S6. Drawing a line between point A (apex of crack tip) and point B (bottom of the notch profile).

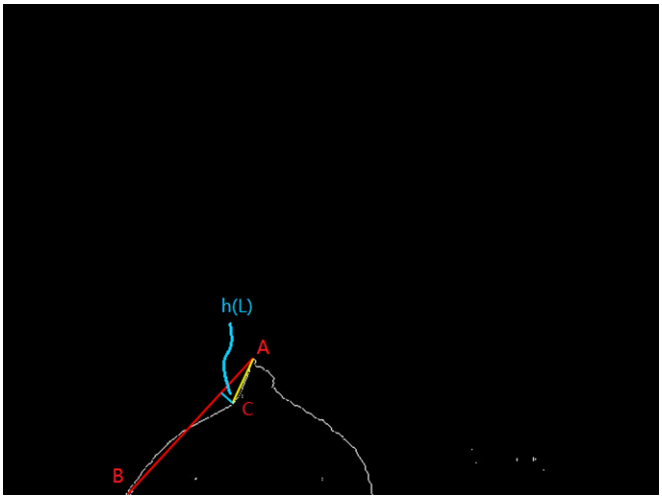

Fig. S7. Final step in extracting crack length.

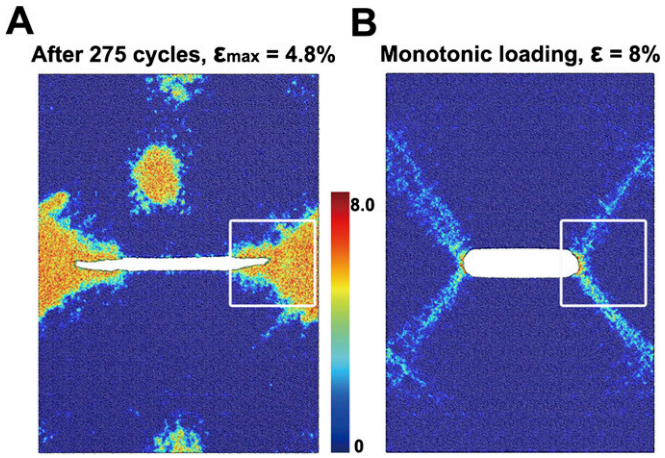

Fig. S8. MD simulations of the distribution of atomistic nonaffine displacement (D^2) in $Al_{50}Fe_{50}$ metallic glass under cyclic straining and monotonic loading. The two samples simulated were of exactly the same geometry with an internal central crack. The color bar shows the intensity scale of D^2 for both samples in units of Å^2. (*A*) The crack propagated quickly after 275 cycles with cyclic strain fluctuating within 3 ± 1.8%. The area framed by the white box shows the active atomic nonaffine movements localized in the fatigue crack tip zone. (*B*) The sample was subjected to 8% monotonic strain that was accommodated without obvious crack propagation. The area framed by the white box indicates that the nonaffine displacement preferentially was along the maximum shear direction.

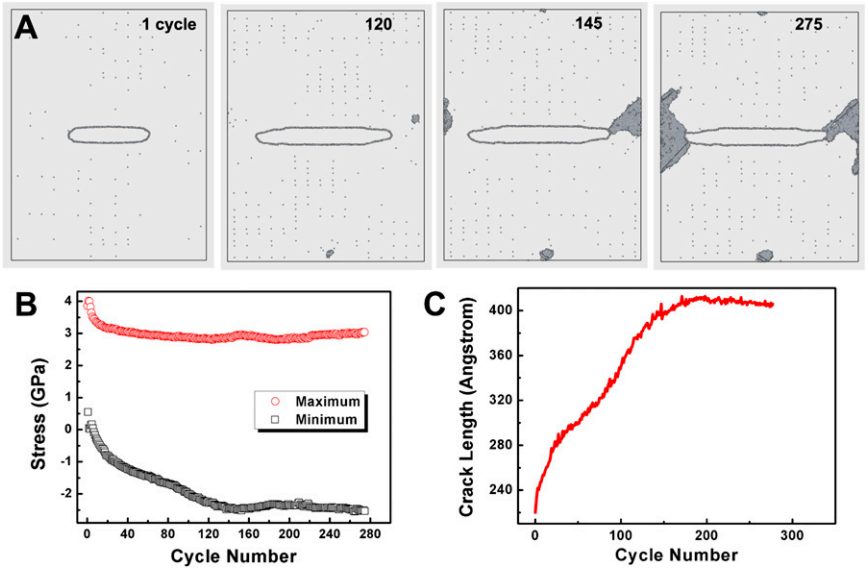

Fig. S9. MD simulation of the cycle-induced crystallization and grain growth in $Al_{50}Fe_{50}$ MG. (*A*) The atomistic configuration of coordination number [only atoms with coordinate number (CN) = 14 are visible] after different cycles (at peak strain). The crack increases rapidly without obvious crystallization for the first 110 cycles. However, a crystal phase nucleates on the right side of the fatigue crack and grows rapidly until reaching the tips of the fatigue crack. (*B*) The evolution of cyclic stress during strain cycling. (*C*) Fatigue crack length increases rapidly in the first 150 cycles, and then it begins to decrease gradually after reaching a peak. Note that the trend observed in MD is very similar to that found in our experiments (Fig. 3 in the main text).

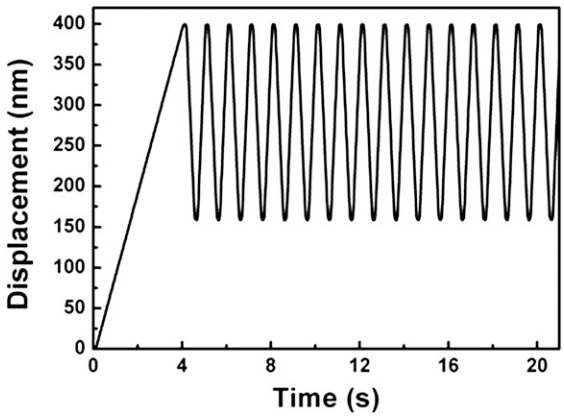

Fig. S10. Displacement-controlled cyclic straining testing with a frequency of 1 Hz and the triangular waveform used in all of the fatigue experiments reported in this work for the test geometry shown in Fig. 1*A* of the main text.

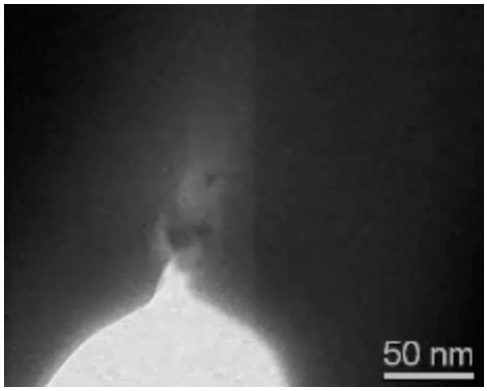

Movie S1. In situ observation of crystallization in Al-based MG beam resulting from cyclic straining inside a TEM.

Movie S1

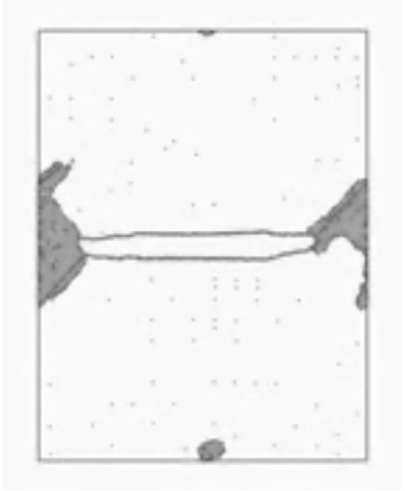

Movie S2. Atomistic configuration of the crystallization process in MG from molecular dynamics simulation.

Movie S2